

Article

Petrology and Geochemistry of an Unusual Granulite Facies Xenolith of the Late Oligocene Post-Obduction Koum Granodiorite (New Caledonia, Southwest Pacific): Geodynamic Inferences

Dominique Cluzel ^{1,*}, Fabien Trotet ² and Jean-Louis Paquette ^{3,†}

¹ Institut de Sciences Exactes et Appliquées (ISEA), University of New Caledonia, BP R4, Nouméa Cedex 98851, New Caledonia

² Centre National de Recherche Technologique Nickel et son Environnement, 101 Promenade Roger Laroque, Nouméa Cedex 98857, New Caledonia; fabien.trotet@cnrt.nc

³ Laboratoire Magmas et Volcans, Campus Universitaire des Cézeaux, 6 Avenue Blaise Pascal, 63170 Aubière, France

* Correspondence: dominique.cluzel@unc.nc

† Deceased 2022.



Citation: Cluzel, D.; Trotet, F.; Paquette, J.-L. Petrology and Geochemistry of an Unusual Granulite Facies Xenolith of the Late Oligocene Post-Obduction Koum Granodiorite (New Caledonia, Southwest Pacific): Geodynamic Inferences. *Minerals* **2024**, *14*, 466. <https://doi.org/10.3390/min14050466>

Academic Editor: Alexandre V. Andronikov

Received: 30 March 2024

Revised: 17 April 2024

Accepted: 24 April 2024

Published: 28 April 2024



Copyright: © 2024 by the authors. Licensee MDPI, Basel, Switzerland. This article is an open access article distributed under the terms and conditions of the Creative Commons Attribution (CC BY) license (<https://creativecommons.org/licenses/by/4.0/>).

Abstract: Pressure–temperature estimates of a xenolith found within a post-obduction granodiorite in southern New Caledonia provide evidence for subcrustal, granulite facies, peak crystallisation conditions (ca. 850°C — 8.5 ± 1.0 kbar), followed by isobaric cooling to 700°C , and final decompression with partial rehydration at ca. 650°C — 3.5 kbar. The xenolith, dated at 24.7 Ma (U-Pb zircon), i.e., the same age as the granodiorite host rock, has low SiO_2 (35.5 wt%) and high Al_2O_3 (33.2 wt%) contents, suggesting that it is the restite of a previous melting episode, while the elevated Ca (Ba and Sr) contents suggest mantle metasomatism. Although the concentrations of Rb, K, Ca, Ba, and Sr have been strongly modified, some geochemical (REE patterns and some “immobile” trace element ratios) and isotopic (Sr and Nd isotopic ratios, U-Pb zircon age) characteristics of the granulite facies xenolith are similar to those of the xenoliths found in other Late Oligocene intrusions in southern New Caledonia; therefore, this rock is interpreted to be related to an early magmatic episode. The rock protolith was emplaced and equilibrated at the base of the crust where it underwent ductile deformation. Younger ascending magma picked it up and they eventually crystallised together at a shallow crustal level, near the tectonic sole of the ophiolite. The recrystallisation and ductile deformation at ~ 8.5 kbar suggest that a rheological discontinuity existed at about 25–28 km, probably representing the Moho. It is concluded that a continental crust of normal thickness must have existed beneath New Caledonia at about 24 Ma, i.e., 10 Ma after obduction.

Keywords: Southwest Pacific; New Caledonia; obduction; subduction; granitoid; xenolith; granulite facies

1. Introduction

Xenoliths found in igneous rocks are generally representative of either their source region or the rocks that the magma traversed on its way to shallower levels. The New Caledonia Ophiolite, commonly referred to as the Peridotite Nappe [1], is a large ultramafic allochthon [2,3] obducted at the Eocene–Oligocene boundary (ca. 34 Ma) [4,5]. In southern New Caledonia, the base of the Peridotite Nappe is crosscut by Oligocene post-obduction granodiorites and granites (Saint Louis and Koum–Borindi complexes) (Figure 1) that mainly intruded the basement and the serpentinite sole of the ophiolite. The plutons and dykes contain thermally metamorphosed enclaves of the autochthonous sedimentary cover of New Caledonia (e.g., Palaeocene limestone found within the St. Louis granodiorite 4.0/).

and rare inherited zircons) and of the Peridotite Nappe itself, such as listvenite (a talc–chlorite–magnesite–haematite metasperpentinite), which was dragged up from the base of the ophiolite. However, no deep-crustal or upper-mantle xenoliths have been described, and the composition of the deep basement of the ophiolite remains largely unknown. The present crustal thickness of the northern Norfolk Ridge has been diversely evaluated at ca. 32 km [6]; in contrast, CRUST2.0 modelling of the Bouguer anomalies resulted in a calculated thickness of ca. 18 km [7], and seismic tomography has provided an intermediate value of ca. 25 km [8]. In addition, to explain the positive Bouguer anomaly (ca. +100 mGal) located in the south of the Grande Terre (Massif du Sud), it has been suggested that the Peridotite Nappe may overlie previously unroofed upper-mantle rocks [9,10]. However, pre-obduction-Palaeocene-to-mid-Eocene pelagic limestone that uniformly covers the northern Norfolk–New Caledonia Ridge suggests a continental crust thickness of about 20–25 km just prior to obduction. A similar crust thickness and carbonate cover have been established for the Lord Howe Rise, which was once continuous with the Norfolk Ridge [11,12]. The occurrence within the Late Oligocene granodiorite of rare inherited zircons coming from Late Cretaceous sandstones [13] and the xenoliths of Palaeocene pelagic limestone suggest that the sedimentary cover extends below the ophiolitic allochthon. Alternatively, the local gravity anomaly has been interpreted as being related to a post-obduction transtensional graben, along the borders of which the Oligocene granitoids were emplaced [14].

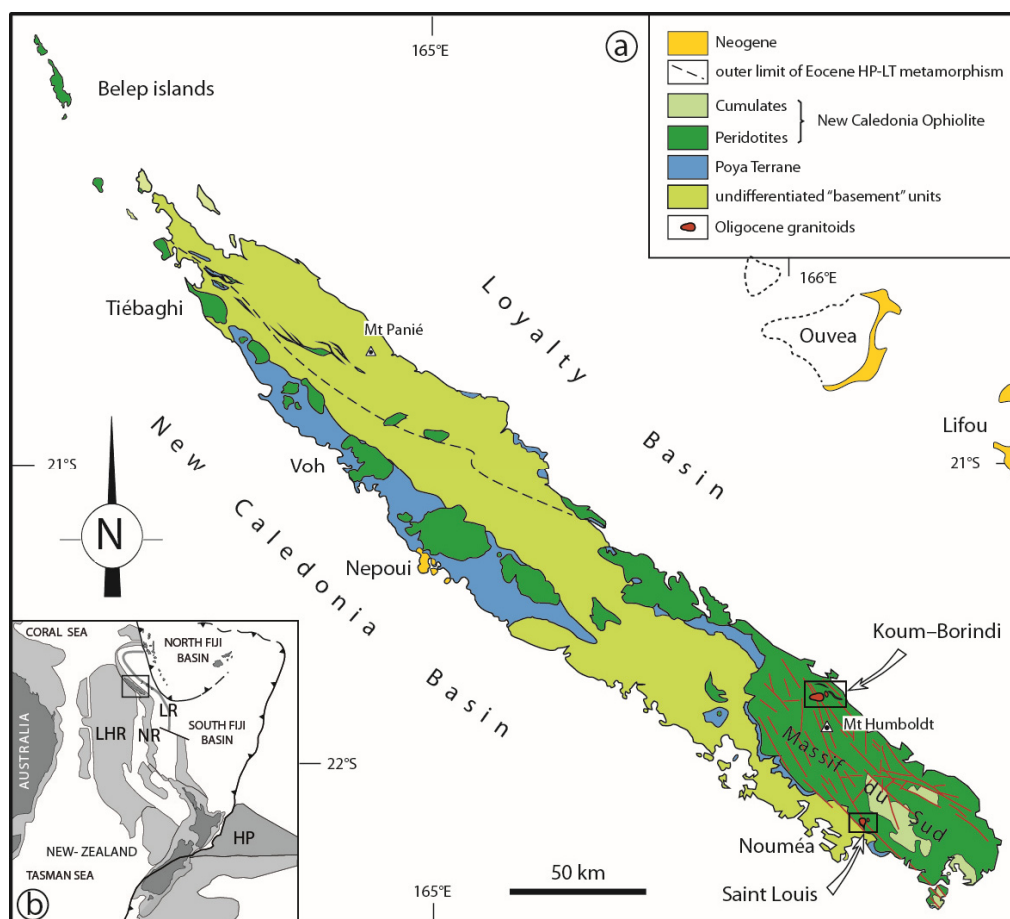


Figure 1. (a) Geological sketch map of the Tertiary allochthons of New Caledonia, with the locations of the two main Oligocene granitoid occurrences at St. Louis and Koum–Borindi that crosscut the ultramafic allochthon (Peridotite Nappe) in the southern part of the island. (b) Sketch map of the SW Pacific. Dark grey: land; light grey: thinned continental crust areas (submerged); white: oceanic crust areas. LHR: Lord Howe Rise; NR: Norfolk Ridge; LR: Loyalty Ridge; HP: Hikurangi Plateau.

This article presents a reappraisal of the granulite facies rock found as a xenolith in the Koum granodiorite, which has been dated at 24.7 ± 0.2 Ma (U-Pb zircon) and only superficially described [13]. It is based mainly upon mineral microprobe analyses and a tentative evaluation of the pressure–temperature path. This is the only record of a high-grade xenolith from the Late Oligocene granitoids of New Caledonia, and it is of some importance for our knowledge of the basement of the northern termination of the Norfolk Ridge, which is otherwise poorly known due to its overall submarine nature. In particular, an estimate of the crustal thickness beneath the northern Norfolk Ridge is expected. We investigated the unusual nature of this xenolith found within the Koum–Borindi intrusive complex (long. 166.3788, lat. -21.7554) along the upper reaches of the Xwe Fachia (river), 55 km to the north of Noumea.

2. Material and Methods

The mineral composition of the biotite, garnet, plagioclase, hercynite, muscovite, and chlorite were determined using a Cameca SX50 electron microprobe (15 keV, 20 nA) at the BRGM-CNRS-University of Orleans analytical pool. Approximately 250 mineral analyses were performed using four polished, thin sections of the xenolith. Only a few representative analyses are included in this paper (Table 1); the complete data set is presented in the Supplementary Materials (Table S2). The mineral formulae presented in the following section are the averages taken when the variation in the elemental content remains within the range of analytical errors ($\pm 5\%$). A qualitative chemical analysis of the very fine-grained accessory phases (zircon, magnetite, ilmenite, allanite, monazite, and xenotime) was carried out by backscattered electron EDS on a JEOL 6400 SEM at the Polytech’s analytical facility (University of Orleans, Orleans, France). Whole-rock major (ICP-OES), trace element (ICP-MS), and Nd-Sr isotope analyses of the granulite facies xenolith BOR5 [13] were carried out at the Service d’Analyse des Roches et Minéraux (CNRS-CRPG Nancy, Nancy, France); the analytical procedures, errors, and detection limits can be found at <https://sarm.cnrs.fr/index.html> (accessed on 15 June 2006). Whole-rock geochemical and isotopic data for Late Oligocene granitoids are from [14].

Table 1. Electron microprobe analyses of representative mineral phases. Biotite analyses marked by an asterisk have been recalculated by integrating the exsolution of Fe-Ti oxides.

Data Point	Mineral	SiO ₂	TiO ₂	Al ₂ O ₃	Cr ₂ O ₃	FeO	MgO	MnO	NiO	CoO	CaO	Na ₂ O	K ₂ O	Total %
136	biotite I	31.44	2.39	19.21	0.00	21.68	8.30	0.03	0.00	0.20	0.04	0.49	7.35	91.13
136 *	recalc	28.30	7.13	17.29	0.00	24.24	7.48	0.09	0.00	0.19	0.03	0.44	6.62	91.81
106	biotite I	33.43	1.54	18.35	0.07	22.20	9.08	0.02	0.09	0.03	0.02	0.67	7.81	93.28
106 *	recalc	30.09	6.36	16.52	0.07	24.70	8.18	0.08	0.08	0.03	0.02	0.60	7.03	93.75
3	biotite II	32.66	2.35	19.09	0.00	21.55	8.63	0.15	0.00	0.00	0.05	0.64	7.39	92.50
150	biotite II	32.95	1.76	18.29	0.00	20.31	9.55	0.15	0.17	0.00	0.09	0.81	7.29	91.35
13	Plagio I	43.74	0.03	35.75	0.00	0.12	0.00	0.00	0.05	0.01	19.25	0.27	0.00	99.21
137	Plagio I	43.52	0.00	35.62	0.04	0.12	0.00	0.10	0.00	0.00	19.74	0.12	0.02	99.28
9	Plagio II	44.5	0.00	36.2	0.00	0.00	0.00	0.03	0.00	0.00	19.3	0.45	0.01	100.5
33	Plagio II	44.2	0.00	36	0.00	0.13	0.00	0.00	0.00	0.00	19.5	0.37	0.03	100.2
25	hercynite	0.09	0.00	54.76	0.05	41.98	2.73	0.34	0.00	0.00	0.00	0.04	0.00	99.99
148	garnet	37.88	0.01	21.36	0.00	32.33	3.79	2.03	0.11	0.01	3.37	0.01	0.00	100.90
138	garnet	37.32	0.06	21.44	0.01	32.17	3.71	1.88	0.20	0.00	3.54	0.01	0.01	100.36
46	margarite	30.67	0.00	50.21	0.00	0.61	0.13	0.07	0.04	0.01	12.17	0.65	0.02	94.59
119	margarite	30.38	0.00	50.36	0.00	0.52	0.10	0.00	0.03	0.08	12.86	0.41	0.00	94.75
42	epidote	39.52	0.01	31.27	0.00	1.32	0.01	0.00	0.00	0.06	23.01	0.01	0.05	95.24
120	epidote	38.62	0.00	29.19	0.00	5.62	0.02	0.03	0.00	0.10	22.92	0.04	0.03	96.55
158	K mica	43.25	0.00	35.24	0.00	1.19	0.29	0.07	0.00	0.01	0.01	0.15	10.28	90.50
54	chlorite	24.06	0.00	23.27	0.02	27.47	12.04	0.16	0.00	0.05	0.05	0.01	0.02	87.13
126	Fe chlorite	22.41	0.00	23.68	0.00	34.38	7.33	0.10	0.00	0.00	0.08	0.00	0.00	87.98

3. Geologic Setting

One of the main geological features of New Caledonia is the ultramafic allochthonous terrane [2] known as the Peridotite Nappe [1], which was obducted in the latest Eocene or earliest Oligocene period and thrust over the northern tip of the Norfolk ridge, as the latter obliquely entered into the subduction zone of the intra-oceanic Loyalty volcanic arc [14]. The ophiolite consists of a strongly depleted harzburgite–dunite suite, 2500 m thick at most, overlayed by a 200 to 500 m thick dunite transition zone, associated with chromite pods and mafic–ultramafic cumulate lenses [5,15–17]. As a result of the Eocene subduction being blocked by continental crust elements, a new subduction started for a period along the west coast of New Caledonia, producing the Late Oligocene granitoids of St. Louis (west coast) and Koum–Borindi (east coast) at ca. 24.5 Ma [13,14] (and new unpublished U-Pb zircon data) (Figure 1). The Oligocene granitoids are intruded in the autochthonous basement and in the lowermost levels of the Peridotite Nappe. The Koum granodiorite is part of the Koum–Borindi intrusive complex, which consists of several hecto-to-kilometre-scale felsic intrusive bodies and dykes emplaced in a fault-crossing zone along the boundary of a post-obduction transtensional graben containing the cumulate lenses (Figure 1).

The St. Louis and Koum–Borindi intrusive rocks are volcanic-arc granites [18,19], which show little geochemical variation due to differentiation and/or source diversity (Supplementary Materials Table S1). However, two main geochemical types have been distinguished on the basis of their REE contents: a “normal” type (I), comprising about 80% of the analysed samples from both intrusive complexes, and an HREE-depleted type (II) restricted to Koum–Borindi (Figure 2) [14].

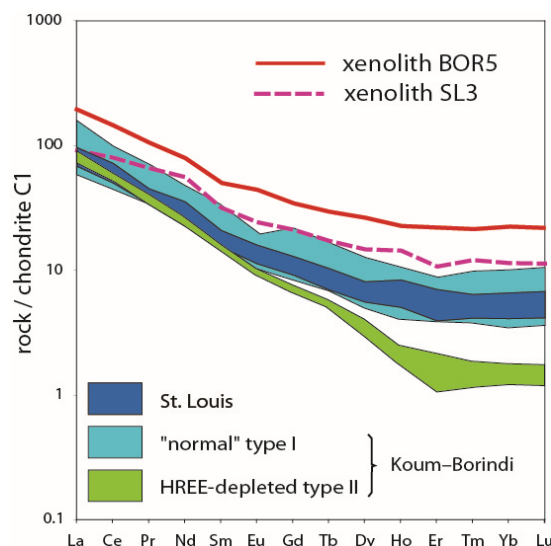


Figure 2. Rare earth elements pattern of the granulite facies xenolith BOR5 compared with the St. Louis granitoids and the two rock types (“normal” and HREE-depleted) that form the Koum–Borindi intrusive complex. The restitic xenolith SL3 from St. Louis is moderately depleted in REE compared to BOR5.

Various hypotheses have been put forward about the origin of these granites: (1) subduction related [14], (2) delamination of the lithosphere [20], and (3) slab melting [21]. Although none of these interpretations is entirely satisfactory, and some are based on limited, not to say erroneous, data, this article is not intended as a reappraisal of granitoid origin. Rather, because of the diversity of processes involved in granitoid genesis [22,23], we have used the occurrence of the granulite facies xenolith as a supplementary constraint on the existing model.

Only 13% of the Late Oligocene granitoid samples have $\text{Sr}/\text{Y} > 40$ and could, therefore, be recognized as adakites, s.s., according to the original definition [24]; however, according

to a less restrictive classification [25], up to ~78% of the samples could be considered as adakite-like rocks ($\text{Sr}/\text{Y} > 20$) (Figure 3a).

The relatively high Sr/Y ratios and HREE depletion could be viewed as a consequence of the variable amounts of garnet in their source [26]. The HREE depletion ($(\text{La}/\text{Yb})_{\text{N}} > 40$) of some of the rocks in the Koum–Borindi complex (Type II granitoids) (Figure 3b) suggests the involvement of the lower crust in magma genesis [27]. Overall, such features may be due to the interaction between slab melts, the supra-subduction mantle wedge, and a mafic garnet-bearing lower crustal source [25,28]. It is worth noting that the intrusion period (24.5 Ma) coincided with a pronounced uplift of New Caledonia, as indicated by regolith erosion and rapid granitoid uplift and/or cooling at c. 24–22 Ma (zircon U-Th/He) (Zhou R. Univ. of Queensland pers. comm.), which can be interpreted as a result of slab break off [29]. Despite granitoid intrusion within the basement rocks of the Norfolk ridge, no noticeable geochemical or isotopic contamination by continental crust rocks has been detected [14] (see isotope data below).

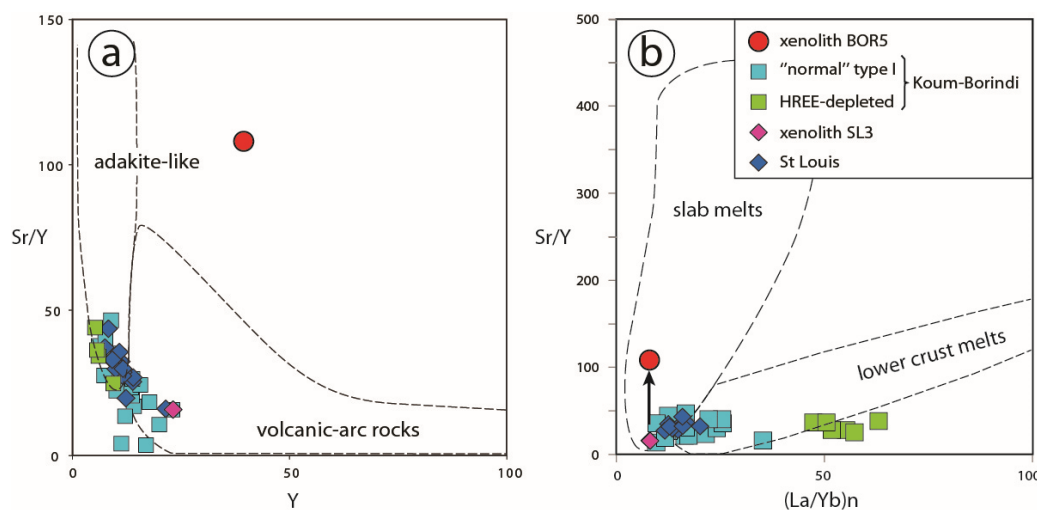


Figure 3. (a) Sr/Y vs. Y diagram [24] showing the relatively low Sr/Y ratios of most Oligocene granitoids. (b) Sr/Y vs. $(\text{La}/\text{Yb})_{\text{n}}$ diagram [24,27] showing the similarity of the St. Louis and Koum–Borindi granitoids, except for the HREE-depleted type, which was strongly influenced by lower crust melts. The restitic xenolith SL3 from St. Louis shows an unchanged Sr/Y ratio, in contrast to the strong Sr (Ba and Ca) metasomatism of the granulite BOR5, which is also evident from multi-elements patterns.

4. Analytical Results

4.1. Mineralogy and Petrography

The studied granulite facies xenolith is a dark granular rock; 20 cm × 10 cm in size; lacking any mineral shape-preferred orientation; and composed of plagioclase, garnet, biotite, and hercynite as the primary phases; and margarite, epidote, “sericite”, chlorite, minor calcic amphibole, calcite, and celsianite as the secondary phases. The accessory minerals include zircon, magnetite, ilmenite, allanite, monazite, and xenotime.

- Plagioclase is the major mineral phase, consisting of 1–3 mm unzoned and inclusion-free grains. The larger grains display sub-grains of 200 µm on average, with the same optical orientation, giving them a mottled appearance (e.g., Figure 4j). This sub-grain texture is probably due to annealing.
- The biotite consists of 2–4 mm globular, sometimes gently kinked crystals and smaller decussate flakes, averaging 50–400 µm, interspersed within plagioclase grains. The larger biotite crystals (biotite I) contain 10%–15% small, granular opaque minerals (predominantly ilmenite) forming concentric aureoles (Figure 4a), and ilmenite exsolution needles geometrically arranged along the crystallographic directions. As with the smaller flakes, the outer rim of the large biotite grains is typically free of opaque

inclusions (biotite II) (Figure 4a,b). Hercynite never occurs as inclusions in biotite I, but small garnet grains do; occasionally, minute hercynite grains may be found within biotite II flakes. Within hercynite–biotite aggregates, biotite II is often replaced by chlorite.

- The garnet consists of typically poikiloblastic almandine grains with a few plagioclase, biotite, hercynite, and Fe oxide inclusions (Figure 4c,d). The low pyrope content ($Mg/Fe_{tot} = 0.2$) is probably due to the low Mg bulk rock composition (see below). Some garnet grains contain sinuous trails of elongated, opaque mineral inclusions (Fe oxide, Figure 4c) and are, therefore, similar to synkinematic garnets developed in regionally metamorphosed rocks. However, no other mineral in the rock shows similar syntectonic features, and post-kinematic recoil is likely.
- The hercynite (Fe-Al spinel) occurs as irregular aggregates 2 to 4 mm in size, consisting of 50–250 μm subhedral, dark-green grains, with interstitial biotite (50 μm) often destabilised into chlorite (Figure 4e). Irregular hercynite aggregates are likely to have come from the destabilisation of an older mineral phase, but no relicts were found and the existence of an earlier paragenesis remains conjectural. The boundary of hercynite aggregates with plagioclase is formed by a microgranular destabilisation aureole formed of corroded plagioclase grains, margarite, epidote, K-rich white mica (“sericite”), chlorite, and minor calcite (Figure 4e–h).
- Anorthite-rich plagioclase I, garnet, and biotite I display inclusions of each other, have no reaction boundary (Figure 4d) and, therefore, appear likely to be paragenetic.
- Colourless acicular crystals of margarite are organised in sheaf-like aggregates (Figure 4g). In the distal part of some aggregates (toward the plagioclase), the margarite transitions into and is intergrown with poorly crystallized muscovite (sericite) (Figure 4g,h and Figure 5d). At the boundary between the margarite and plagioclase grains, anorthite-rich plagioclase I is locally altered to a lower Ca plagioclase (plagioclase II, An 90%), together with the crystallisation of small calcite intergranular blobs. Tiny celsianite grains ($Ba [Si_2Al_2O_8]$) also appear within the destabilisation aureoles and are probably due to Ba exsolution from the Ba-bearing primary plagioclase I.

In contrast to plagioclase I, biotite I, garnet, and hercynite, which occur as primary phases, plagioclase II, biotite II, margarite, sericite, chlorite, calcite, celsianite, and epidote are secondary lower-grade phases within reaction aureoles 200–400 μm thick around hercynite aggregates. Hercynite and plagioclase appear to have reacted together during a lower-grade event, resulting in margarite, chlorite, and K-mica. It is noteworthy that these retrograde minerals are closely associated with allanite–monazite intergrowths (Figures 4i and 5a–c). The destabilisation aureoles around the hercynite aggregates also contain a few xenotime grains associated with sericite, epidote, calcite, and chlorite (Figure 5d).

The epidote and chlorite show complex textural relationships with other phases, being associated either with garnet–plagioclase I–biotite I–hercynite (without reaction features) or with margarite–plagioclase II–sericite assemblages. However, the mineral compositions of the chlorites involved in these two main assemblages are different. It has been shown that variations in chlorite composition can be explained in terms of $FeMg_{-1}$ substitution (between the daphnite and clinochlore end-members), Tschermak substitution (between clinochlore/daphnite and amesite), and di-trioctahedral substitution (between daphnite/clinochlore and sudoite) [31–33]. In particular, the amount of evolution towards the sudoite end-member is indicative of the intensity of retrograde evolution. It should be stressed that several generations of chlorite (resulting from several recrystallization events) may have occurred within the same thin section, but in different microstructural settings.

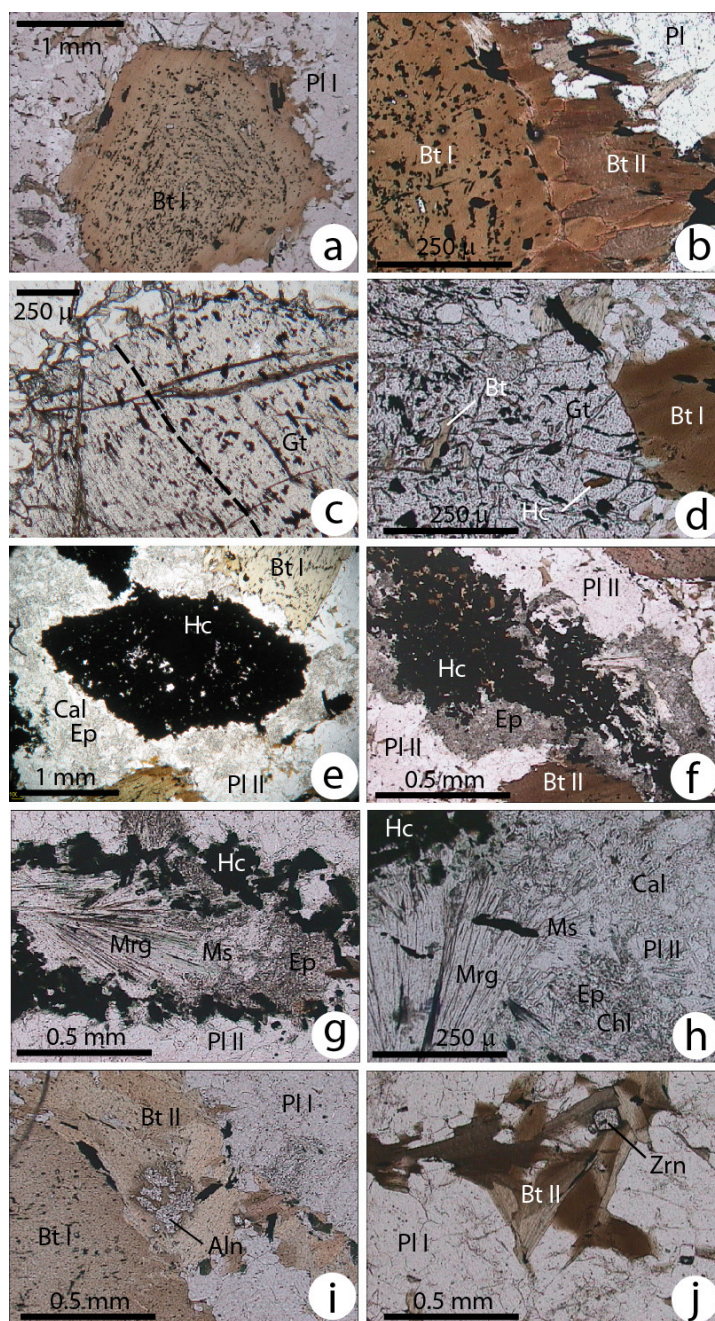


Figure 4. Photomicrographs of the representative textures of the granulite xenolith. Aln: allanite; Bt: biotite; Cal: calcite; Chl: chlorite; Ep: epidote; Gt: garnet; Hc: hercynite; Mrg: margarite; Ms: sericite (fine-grained muscovite); Pl: plagioclase; Zrn: zircon. Mineral abbreviations are from [30]. (a) A large poikilitic biotite I crystal showing a concentric arrangement of ilmenite and magnetite grains due to Fe and Ti exsolution with decreasing temperature; (b) coexisting biotite I (poikilitic) and biotite II (inclusion free); (c) a representative sector of a poikilitic garnet grain containing sinuous, opaque inclusion trails underlined by the dotted line; (d) in-equilibrium garnet and biotite I (note the small-sized inclusions of biotite and hercynite); (e) shapeless hercynite aggregate containing light-coloured plagioclase and biotite intergrowths; (f) poorly crystallised epidote, chlorite, margarite, sericite, and calcite reaction rim around hercynite aggregate and against anorthite II plagioclase; (g) sheaf-like margarite aggregate with sericite and epidote at the end surrounded by hercynite grains and plagioclase; (h) detail of a margarite aggregate showing the complex intergrowth of sericite, chlorite, epidote, and calcite; (i) a large (250 μm) lacunar allanite enclosed in a biotite II flake; (j) decussate aggregate of biotite II flakes associated with an automorphic zircon crystal.

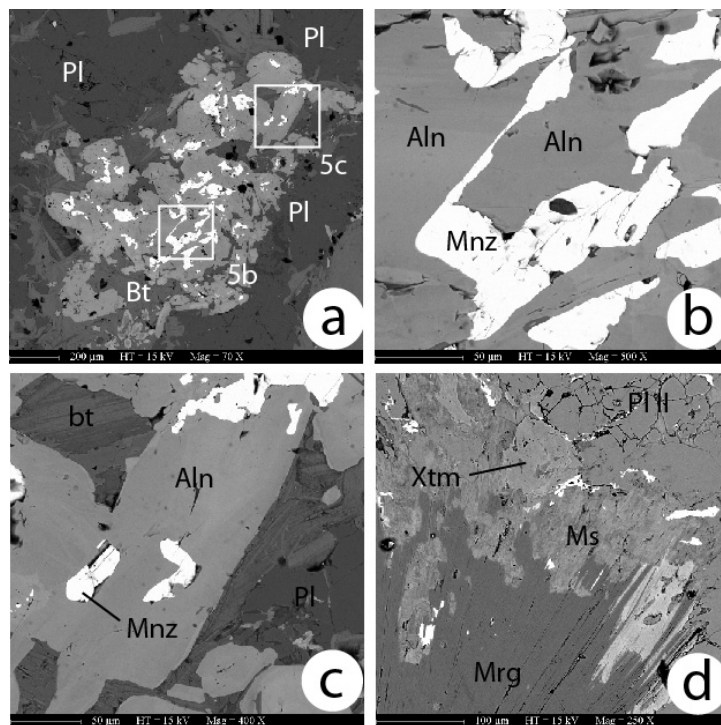


Figure 5. SEM pictures of REE-bearing minerals. (a) Allanite and monazite intergrowths associated with plagioclase and biotite; (b,c) enlarged parts of (a) showing details of allanite and monazite intergrowths; (d) xenotime grain in the distal part of a margarite and sericite sheaf.

4.2. Mineral Compositions

Two generations of plagioclase have been distinguished on the basis of the textural relationships (see above), the first forming the bulk of the rock and belonging to P1. Plagioclase I is an almost pure anorthite (An 99%) with no chemical zoning. The second generation (plagioclase II) occurs in reaction zones associated with margarite, calcite, and celsianite; it is, nonetheless, an anorthite, but with a lower Ca content (An 90%) (Supplementary Materials Table S1).

The biotite compositions ($(K_{0.78}Na_{0.09})(Fe_{1.43}Mg_{1.05})(Al_{0.36}Ti_{0.12})[Al_{1.4}Si_{2.6}O_{10}](OH)_2$) are close to the siderophyllite (Fe-rich) pole of the siderophyllite–eastonite aluminous solid solution [34]. There is no difference in chemical composition between the larger biotite grains and the smaller flakes; however, given the importance of ilmenite exsolution within the larger grains, a more Ti-rich biotite probably formed at an early stage of crystallisation (P1) and released Fe-Ti oxides during recrystallization at lower temperatures, while second-generation biotite flakes appeared (P2). A recalculation of the chemical composition of biotite I based on modal composition using image analysis (10% modal ilmenite) and microprobe data suggests that biotite I was originally a titaniferous siderophyllite ($(K_{0.69}Na_{0.09})(Fe_{1.63}Mg_{0.92})(Al_{0.02}Ti_{0.43})[Al_{1.62}Si_{2.36}O_{10}](OH)_2$) (Figure 6a,b), which may be stable in granulite facies conditions (see below). In contrast, biotite II probably represents the re-equilibration of biotite I at lower temperatures and newly crystallized material [35].

The garnet grains are not zoned and typically consist of almandine (Alm 78.7%, Pyr 16.6%, Spes 4%, on average; or $(Fe_{2.12}Mg_{0.45}Mn_{0.12}Ca_{0.30})[Al_2Si_3O_{12}]$) (Figure 6c). A low pyrope content ($Mg/Fe_{tot} = 0.2$) is due to the low Mg bulk rock composition (2.65 wt% MgO; see below).

The hercynite shows very constant chemical composition close to the ferrous end-member $(Fe_{0.87}Mg_{0.12}Mn_{0.01})(Al_{1.90}Fe^{3+}_{0.14})O_4$.

With only a few exceptions of very Fe-rich flakes, the chlorites plot at the boundary between the Corundophyllite and Pseudothuringite domains (Figure 6d) is due to the high Fe/Mg ratio of the original biotite mother mineral.

The margarite is an almost pure calcic end-member ($(\text{Ca}_{0.9}\text{Na}_{0.1})\text{Al}_2[\text{Al}_{1.97}\text{Si}_{2.03}](\text{OH})_2$) with less than 10% Ca-Na substitution; its composition shows no variation either along the c axis of the prisms, nor from one aggregate to another.

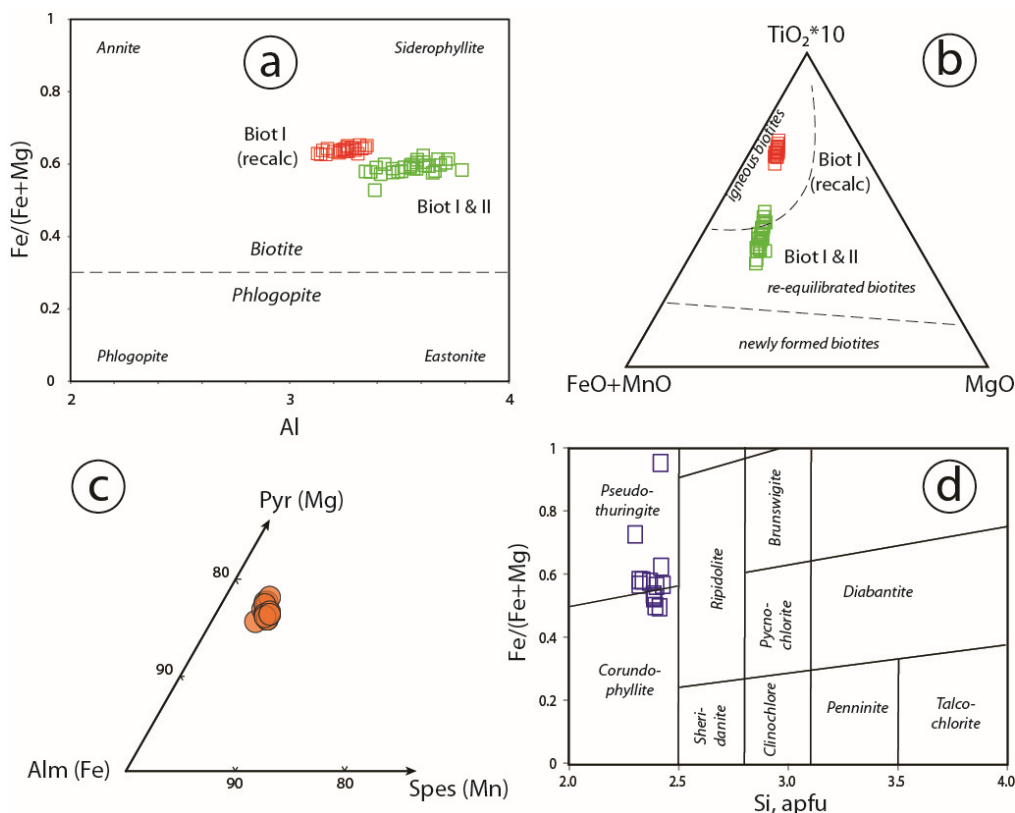


Figure 6. Mineral classification. (a) Fe-Mg-Al biotite classification diagram [34]; (b) Fe-Mn-Mg-Ti ternary diagram [35] shows biotite I plots in the domain of magmatic biotites, and biotite II in the domain of re-equilibrated biotites; (c) garnet triangular classification diagram; (d) FeMg-Si classification diagram for chlorites [36].

4.3. Thermobarometry

The BOR5 sample is obviously not a common granulite, as it has an atypical bulk composition that precludes the use of classical geothermometers (e.g., garnet–clinopyroxene, garnet–hornblende) or geobarometers (e.g., garnet–plagioclase–hornblende–quartz). Furthermore, in the six-components system $\text{K}_2\text{O}-\text{CaO}-\text{MgO}-\text{Al}_2\text{O}_3-\text{SiO}_2-\text{H}_2\text{O}$, seven solid phases are needed to obtain an invariant assemblage if each solid phase is modelled as a single phase component (or end-member). The sample contains a large number of components, but only a few phases are shown to coexist at equilibrium due to incomplete recrystallisation. Overall, SiO_2 is not in excess in this sample, and this infers that quartz cannot be involved in phase equilibria. For these reasons, most of the parageneses observed are divariant. However, the ability to resolve pressures and temperatures can be improved by increasing the number of end-members used to express the compositional variability of the phases in a given paragenesis (multi-equilibrium calculation) [37,38]. Calculations involving such models provide a simultaneous estimate of pressure and temperature (even for high-variance parageneses), which can be interpreted in terms of P-T conditions at equilibrium for a given paragenesis (i.e., P-T conditions of crystallization). This approach has been successfully used by various researchers [32,33,38–41]. The end-member standard-state thermodynamic properties and solid–solution models (except for chlorite) are from the JUN92 database associated with TWEEQU 1.02 software [37]. The chlorite solid–solution model, as well as the internally consistent standard-state thermodynamic properties for daphnite, Mg–amesite, and Mg–sudouite, are from [31]. The activity of epidote was calcu-

lated according to [42]. The activities of hercynite and H_2O were assumed to be unity, as discussed below.

Parageneses were selected using classical petrographic criteria, i.e., the habit of the minerals, their textural relationships (straight grain boundaries between minerals, no evidence of reaction between mineral phases), and their microstructural setting (site where minerals are believed to have crystallized simultaneously). In addition, the following criterion derived from the multi-equilibrium thermobarometric method was used. The disequilibrium between minerals used to make a P-T estimate result in a significant scatter of the intersections between the equilibrium reactions (σP and σT calculated with IntersX [37]). It was suggested [32] that the maximum allowable scatter ($\sigma\text{P}_{\text{max}}$, $\sigma\text{T}_{\text{max}}$) of any P-T estimate (although paragenesis dependent) is $\sigma\text{P}_{\text{max}} = 800$ bars, $\sigma\text{T}_{\text{max}} = 25$ °C. If $\sigma\text{P} < \sigma\text{P}_{\text{max}}$ and $\sigma\text{T} < \sigma\text{T}_{\text{max}}$, the scatter could be due to microprobe imprecision. Alternatively, if $\sigma\text{P} > 800$ bar or $\sigma\text{T} > 25$ °C, the minerals are considered to be out of equilibrium, and the P-T estimate is rejected. The calculated scatter (σP and σT) is, therefore, the final criterion used to assess the state of equilibrium achievement for a given mineral assemblage. Several studies have highlighted that the textural and chemical (quality of the microprobe analyses) criteria for equilibrium correlate quite well with the results of P-T calculations, in which equilibrium is inferred from the convergence of the intersections in the P-T field [32,33,38].

In the BOR5 sample, we have identified the paragenesis P2 (garnet–plagioclase II–biotite II–hercynite–epidote–chlorite) as suitable for multi-equilibrium calculations. In the seven-component system $\text{K}_2\text{O}-\text{CaO}-\text{FeO}-\text{MgO}-\text{Al}_2\text{O}_3-\text{SiO}_2-\text{H}_2\text{O}$, using eleven phase components (daphnite, amesite, clinochlore, phlogopite, almandine, pyrope, anorthite, annite, clinozoisite, hercynite, and water), we can calculate thirty-nine reactions, four of which are independent. Similar calculations made for the same paragenesis, found at different locations of the BOR5 sample, gave similar results in the range of 695 to 683 °C and 8.4 to 7.4 kbar (e.g., Figure 7).

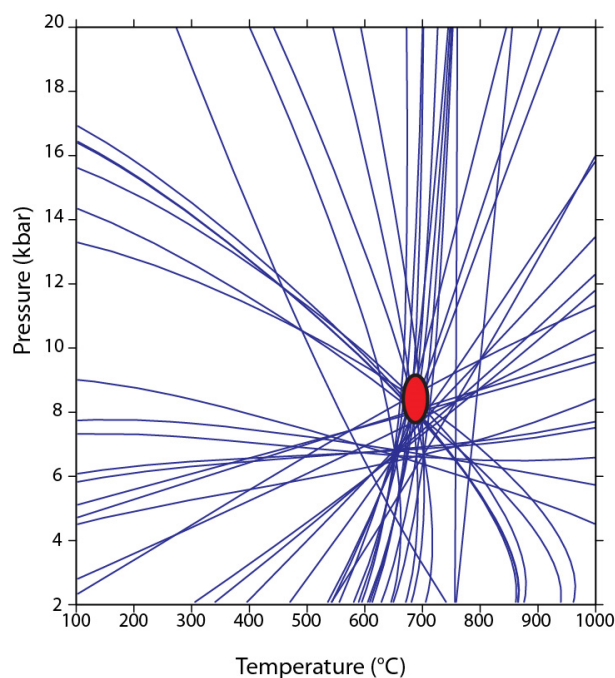


Figure 7. An example of multi-equilibrium thermobarometric calculation for metamorphic assemblages identified as (equilibrium) parageneses in thin section. Thirty-nine reactions were calculated and four of them are independent. The calculation results show little scattering of the different P-T intersections, suggesting equilibrium between minerals, and are consistent with the textural observations. The molar fractions of the cations per site in the plagioclase, chlorite, garnet, and biotite (see text for solid–solution models) used in the calculations are shown below.

PLAG	[-An-]	[-Ab-]	[-Or-]						Borindi 82
PLAG	0.968	0.032	0.000						
CHL	[-xsi]	[-xAl]	[-xMg]	[-xFe]	[-xAl]	[-xV]	[-xMg]	[-xFe]	Borindi 74
CHL	0.286	0.713	0.250	0.274	0.431	0.045	0.466	0.509	
GARN	[-Gr-]	[-Py-]	[-Alm]	[-Sp-]					Borindi 75
GARN	0.096	0.141	0.725	0.038					
BIOT	[xMg-]	[xFe-]	[-xTi]	[-xAl]	[-xK-]	[xOH-]			Borindi 76
BIOT	0.339	0.484	0.045	0.164	0.760	0.999			

The peak paragenesis P1 (garnet–plagioclase I–biotite I) cannot be used to estimate the P and T conditions, even using multi-equilibrium calculations. However, the temperature can be calculated from the garnet–biotite equilibrium. High Fe and Ti concentrations can increase the temperature stability of biotite in near-granulite facies conditions [43,44]. We used image analysis to estimate the amount of magnetite and ilmenite exsolution within the biotite I crystals. A subsequent recalculation of the biotite I composition suggested an increase in Ti from 0.03 to 0.09 atoms per formula unit. Thermobarometric calculations using the recalculated compositions of biotite, for garnet + biotite (I) associations found at several sites within the thin section, led to temperature estimates in the range of 800–900 °C at P > 8 kbar.

Given the mineralogical compositions of the Koum–Borindi intrusive rocks, which contain the minimal ten mineral phases that allow for the use of the Al-in-hornblende empirical barometer [45], we estimated the crystallisation pressure (i.e., emplacement depth) of the host rock of the granulite facies xenolith. Based on the hornblende microprobe analysis of five granodiorite samples from the Koum–Borindi intrusive complex (Supplementary Materials Table S3), we obtained a relatively wide range of pressures for amphibole crystallisation, averaging at ca. 3.5 ± 1.5 kbar (Figure 8).

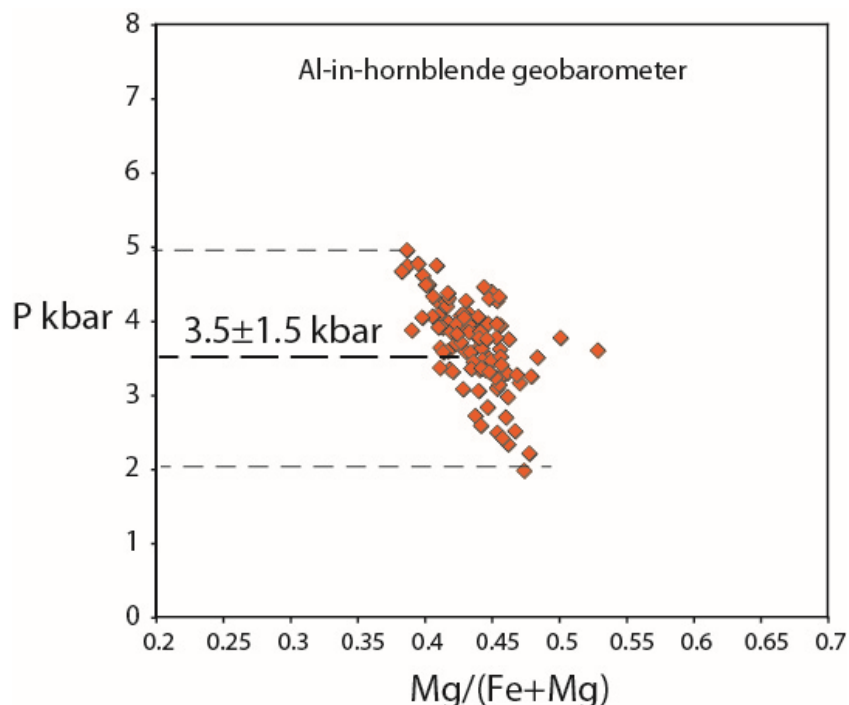


Figure 8. Plot of computed pressures from the Al-in-hornblende geobarometer [45] vs. Mg# ratio. Hornblende compositions were obtained from 5 representative samples (dykes and main body) of the Koum–Borindi complex (Supplementary Materials Table S3).

This result, combined with the P-T geometry of a composite granodiorite–tonalite H₂O-saturated solidus [46–49], provides a rough underestimate of the crystallisation temperature of the intrusion (e.g., [50]), and allows for tentative P-T paths to be constructed, pending a temperature correction to account for H₂O undersaturation (Figure 9). The BOR5 xenolith

was probably first equilibrated in granulite facies (P1) at $P \geq 8$ kbar and underwent ductile deformation, as indicated by the inclusion trails in the garnet. These pressures correspond to a depth of about 28 ± 3 km to 24.5 ± 2.5 km, depending on the average volumetric mass of the overlying rocks, i.e., the ratio of continental crust to obducted upper-mantle peridotite. The first stage of the retrogression path is characterized by an almost isobaric cooling, from about 850 °C to 700 °C. The second stage is characterized by a pronounced decompression path, from ~ 8 kbar and 700 °C to ~ 3.5 kbar and 650 °C. From the present results, it is not possible to rigorously assess whether the exhumation path involved cooling, or alternatively, reheating during decompression, but these results provide additional constraints on the origin of the Borindi granodiorite.

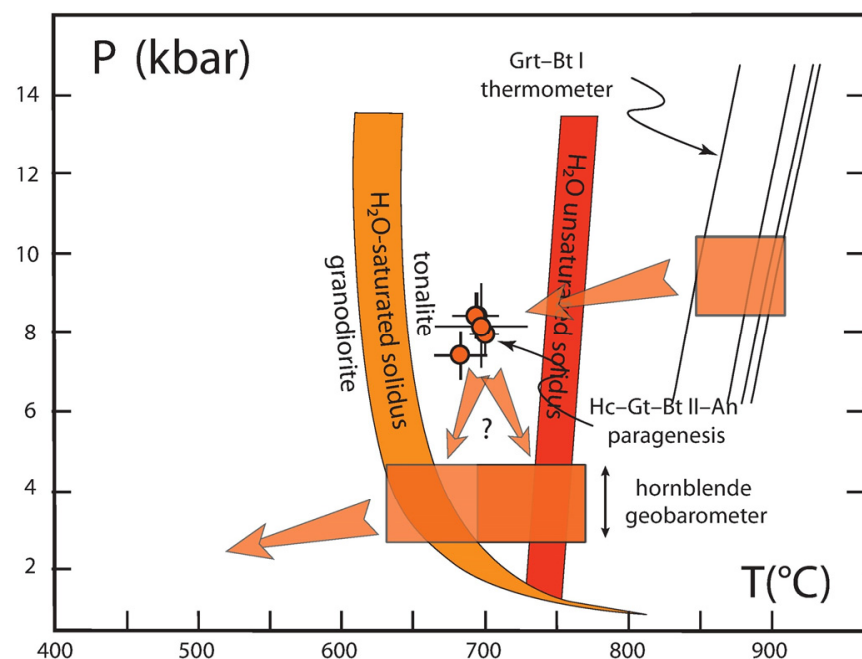


Figure 9. Tentative P-T path derived from the P and T calculated for the granulite facies xenolith BOR5, computed pressure for the host rock (Koum–Borindi granodiorite), crystallisation and granodiorite–tonalite hydrous solidus with a shift towards higher temperatures in the case of a water-unsaturated solidus. The temperature range at the origin takes into account the uncertainty due to Fe–Ti exsolution in the analysed biotite I.

The geological relationships between the xenolith and its host rock suggest that the granodioritic melt originated at depths well below 30 km and ingested lower crustal rocks during its ascent. The xenolith, which initially equilibrated at temperatures ~ 700 °C at the base of the crust, was cooled and partially rehydrated at ~ 650 °C during its ascent to the final emplacement depth of 3–5 km. This is consistent with the geochemical characteristics of the granodiorite, which indicate a volcanic-arc mantle source and only weak subsequent contamination by (Late Cretaceous?) terrigenous sediments [13,14].

4.4. Age Constraints

The age of the main granodiorite body (Grand Koum pluton) host rock of the xenolith was accurately determined to be 24.4 ± 0.1 Ma by U-Pb ID-TIMS on zircons [13]. A new redetermination of the age of another sample of Koum granodiorite by LA-ICPMS gave an identical age of 24.7 ± 0.1 Ma (unpublished data, pers. com. Zhou R. Univ. of Queensland).

The BOR5 xenolith also contains abundant zircons, and four zircon fractions were analysed, giving an identical ID-TIMS age of 24.7 ± 0.2 Ma [13], and none showed evidence of inherited Pb. The complete melting of inherited zircons is only possible in high-temperature magmas, especially those of alkaline composition; in contrast, in calc–alkaline magmas

generated from zircon-bearing rocks, partially melted zircons generally form the core of newly formed grains. Similar U-Pb ages for the zircons of the xenolith and its host rock, and the absence of inherited cores, suggest that the zircons all crystallised at the same time. This, and similar Sr and Nd isotopic ratios indicate that the xenolith was isotopically equilibrated before being raised to the final emplacement level of the pluton.

4.5. Geochemical and Isotopic Features

The chemical composition of the xenolith (Supplementary Materials Table S1) is quite unusual, and many of its geochemical features are somewhat contradictory (see below), reflecting its complicated evolution. Its most prominent whole-rock chemical features are low SiO_2 (35.5 wt%), high Al_2O_3 (33.2 wt%), low K_2O content (1.7 wt%), and very low Na_2O (0.3 wt%) compared to the host rock. The very high Ca (12.6 wt%), Ba (8028 ppm), and Sr (4277 ppm) contents are also unusual. Although it may resemble certain calc-silicate metasedimentary rocks, a sedimentary protolith can be ruled out for the following reasons: (i) such a high Al content is unexpected in calc-silicate metasediments; (ii) the Nd and Sr isotopic ratios (see below) are clearly outside the range of sedimentary rocks; (iii) the abundance of zircon, which is an important accessory mineral phase of the rock, is far too high for a calc-silicate metasediment; and (iv) the zircon population completely lacks rounded or recrystallised grains, and all the grains are idiomorphic and of the same age.

Alternatively, high Al and low Si and alkali contents are common in the restites of felsic magmas and, indeed, the very high Al content is within the range of restitic granulites formed by repeated dehydration and partial melting of the lower continental crust (e.g., [51]). Given the “refractory” nature (Si poor and Al rich) of the granulite facies xenolith, it could be considered as a restite of an underplated source rock. However, the very high Ca, Ba, and Sr contents are not consistent with such a simple interpretation; moreover, such refractory rocks generally have much lower concentrations of incompatible elements (e.g., REE, etc.).

When compared with the Koum-Borindi rocks for their REE and trace elements composition, the multi-element diagram normalised to the primitive mantle [52] of the xenolith (Figure 10) remains close to that of the more evolved granitoids for the LILE-incompatible elements (except Ba and Sr), and three times higher for the HFSE (HREE and Y). The higher content of incompatible elements and the absence of a positive Eu anomaly rule out the cumulate origin of this rock.

A comparison with the SL3 xenolith found in the Late Oligocene St. Louis granodiorite (Noumea area, Figure 1) [13,14] suggests an alternative interpretation. This fine-grained rock has the characteristics of a subvolcanic igneous rock and appears very similar to the xenoliths commonly found in the St. Louis granodiorite. However, unlike other xenoliths that are obviously co-magmatic [14], its geochemical characteristics are clearly different from that of the host rock. In particular, its SiO_2 content (55%) is lower than that of the enclosing St. Louis rocks, which all have SiO_2 contents close to 65%. Its bulk REE content is on average two times higher, while its C1-normalised REE pattern shows less HREE fractionation ($\text{Ce}_n/\text{Yb}_n = 7$) compared to the St. Louis rocks’ range (8.5–14.5). The REE patterns of the two xenoliths are parallel ($\text{Ce}_n/\text{Yb}_n = 6.5$ and 7, respectively), while differing from that of their host rocks. Strikingly, the bulk REE content of BOR5 is twice that of SL3, despite its much lower SiO_2 content (Figure 2). It can be assumed that these xenoliths are both of restitic (igneous) origin, although SL3 appears less refractory than BOR 5 on the basis of the SiO_2 and Al_2O_3 contents alone. On the multi-elements diagrams normalized to the primitive mantle [52], the two patterns also run parallel, but the BOR5 xenolith shows strikingly contrasting features. Its Rb and K contents (and Na, not shown) are strongly depleted, whereas Ba and Sr (and also Ca, not shown) show prominent positive anomalies, and are enriched 5 to 10 times relative to the expected concentrations (Figure 10). The contrasting behaviour of these initially similar rocks can be interpreted as follows. The SL3 protolith was generated at a relatively shallow crustal level and later preserved as a xenolith within the St. Louis granodiorite; in contrast, the BOR5 protolith probably formed

near the base of the crust where it was mineralogically equilibrated in a granulite facies environment, and subsequently incorporated into a younger granodiorite melt.

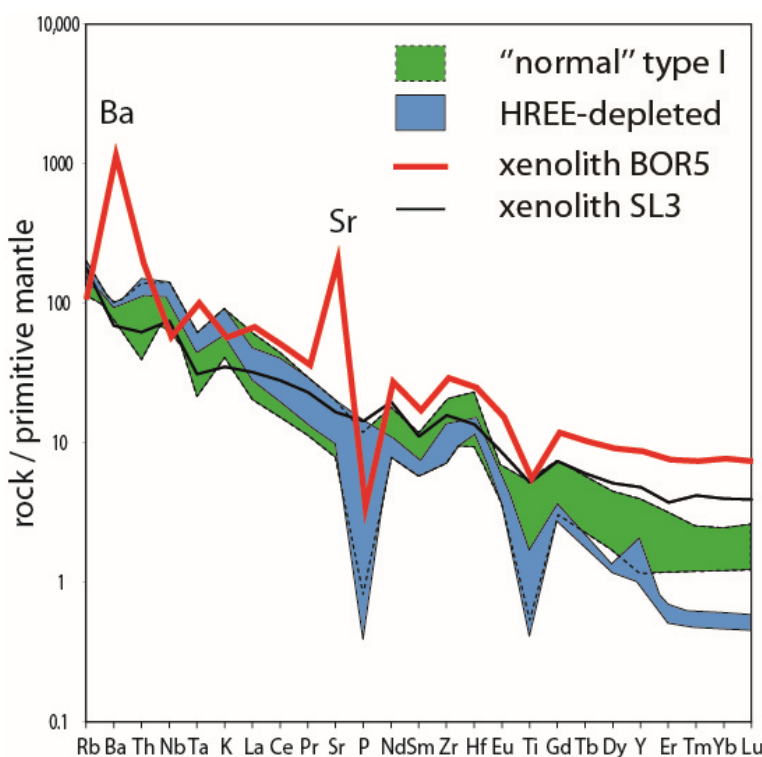


Figure 10. Rare earths and trace elements multi-elements diagram of the Koum–Borindi granitoids (24 sample analyses; [14]) normalised to the primitive mantle [52]. The patterns of the granulite facies xenolith (BOR 5) and the restitic xenolith SL3 (St. Louis) parallel to the “normal” pattern are shown for comparison. Note the relative enrichment of both xenoliths in REE and incompatible elements, and the prominent Ba- and Sr-positive anomalies of the granulite xenolith BOR5.

Isotopic signatures could indicate possible contamination by radiogenic isotopes during the recrystallization of the xenolith. The Nd and Sr isotopic ratios back-calculated at the time of crystallisation (see above) of the granodiorite ($\varepsilon_{\text{Nd}} = +5.1$; $(^{87}\text{Sr}/^{86}\text{Sr}) = 0.70438$) lie within the mantle array and are closely similar to those of the host granodiorite ($+4.8 < \varepsilon_{\text{Nd}} < +5.2$; $0.70366 < (^{87}\text{Sr}/^{86}\text{Sr}) < 0.70438$; Supplementary Materials Table S4) [14], and suggest that the isotopic compositions were re-equilibrated at a high temperature, a result difficult to achieve without a complete remelting of the rock, and inconsistent with its present mineral composition. More simply, the xenolith probably had the same initial isotopic composition as the host rock. A slightly higher $^{87}\text{Sr}/^{86}\text{Sr}$ ratio plotted on the high- $^{87}\text{Sr}/^{86}\text{Sr}$ side of the array formed by the Late Oligocene host rocks (Figure 11) suggests that only very weak contamination by hydrothermal fluids occurred during low-grade recrystallisation and rehydration.

These isotopic features are consistent with the restitic origin of the xenolith proposed above, but do not explain the prominent changes in bulk chemical composition that have occurred. Exploring the conditions of this lower crustal metasomatism is beyond the scope of this article; however, the unchanged isotopic ratios and REE fractionation are inconsistent with a prominent metasomatic input unless the metasomatic source had the same isotopic composition, i.e., that of the moderately enriched mantle. The remarkable amount of REE-bearing accessory minerals associated with secondary parageneses suggests that the REE input occurred synchronously with a moderate pressure drop.

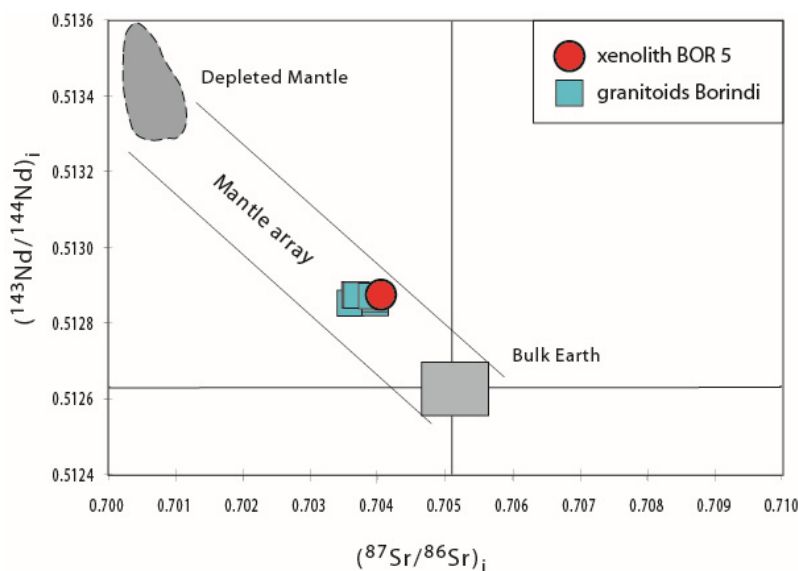


Figure 11. Sr and Nd isotopic ratios of the granulite facies xenolith and host rocks of the Koum-Borindi intrusive complex [14], which emphasise their close similarity and the unchanged $^{87}\text{Sr}/^{86}\text{Sr}$ ratio of the granulite facies xenolith (mantle domains after those in [53]).

This unusual xenolith cannot be considered representative of the lower crust of the Norfolk Ridge, but it could provide evidence for crustal thickness at a given time. Thus, it appears that the crust of the northern Norfolk Ridge was probably ca. 25–28 km thick during the Late Oligocene (c. 24 Ma), which is not greatly different from the pre-obduction thickness in the Palaeocene–Middle Eocene periods (65–42 Ma) inferred from sedimentary facies (see introduction). The hypothesis of significant crustal thinning due to post-obduction gravitational collapse must, therefore, be ruled out, at least in southern New Caledonia. Additional geological evidence, such as the development and preservation of nickel-bearing regoliths by the supergene alteration of peridotite after ca. 25 Ma suggests that the ophiolitic rocks were well above sea level, but did not undergo significant uplift during the Neogene. The development of multiple erosion levels is likely to be due to gentle epirogenic movements and sea level variations [54,55]. It is worth noting that shallow-water marine limestones were deposited during the mid-Miocene along limited coastal areas of western New Caledonia, and did not undergo significant uplift (<50 m). Thus, Neogene extensional exhumation in southern New Caledonia appears to have been gentle, very short lived, and dominated by the break off of the Eocene slab.

5. Summary of Evolution

From c. 56 Ma to c. 34 Ma, the South Loyalty Basin, originally located to the east of the Norfolk Ridge, subducted northeastward and generated the HP-LT metamorphic belt of northern New Caledonia. Subduction blockage by the northern Norfolk Ridge at the end of the Eocene period (Figure 12a) provoked the back jump and initiation of the subduction of the New Caledonia Basin (NCB) (Figure 12b), which accompanied the 60° counterclockwise rotation of the northern Norfolk Ridge [56]. During the NCB subduction, the Late Oligocene granodiorite melts were produced in the mantle wedge, which was variably modified by slab melts. This event probably provoked the underplating of some mafic material, which recrystallized under granulite facies conditions (Figure 12c). Slightly younger granodiorite melt picked up the granulite xenolith and transported it to the lower boundary of the Peridotite Nappe. The subduction of the NCB was eventually blocked by a collision with the Lord Howe Rise, while the continuous downward pull of the Eocene slab provoked its breakoff (Figure 12d). The subsequent delamination of New Caledonia's lithosphere was responsible for moderate uplift, and provided the heat flow necessary to melt already underplated material and form the HREE-depleted granitoids.

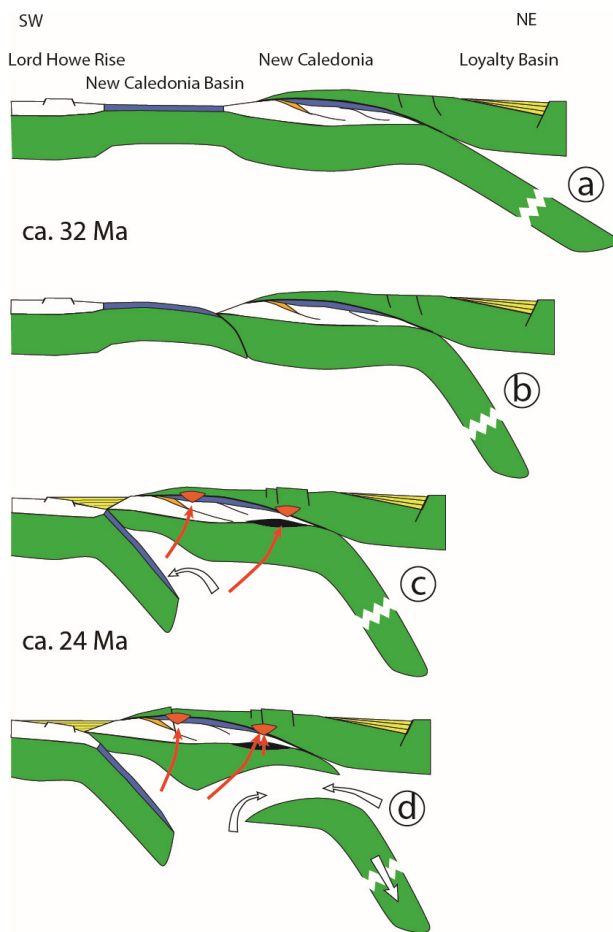


Figure 12. Conceptual model (no scale) for the evolution of New Caledonia during the 32–24 Ma interval. (a) Subduction blockage at the Eocene–Oligocene boundary. (b) Jump back and onset of New Caledonia Basin (NCB) subduction. (c) NCB subduction, intrusion of Oligocene granitoids, and underplating of mafic material. (d) Blocking of subduction by the edge of the Lord Howe Rise, picking up of granulite xenolith, Eocene slab break off, uplift and genesis of HREE-depleted granitoids (lower crust melting). Colour legend: green: mantle lithosphere; blue: oceanic crust; white: continental crust; yellow: post-obduction sediments; red: granitoids; black: underplated mafic material.

6. Conclusions

The granulite facies xenolith BOR5 is probably a restitic magmatic rock that was first equilibrated at subcrustal depth, and thereafter incorporated into the ascending magma. The xenolith shows geochemical evidence for mantle metasomatism, i.e., an increase in Ca, Ba, Sr, REE, etc., without a change in the Nd and Sr isotopic signatures. Such features, and the occurrence of coeval HREE-depleted lower crustal magmas, are consistent with the previously formulated slab-break and mantle-delamination hypothesis. The emplacement depth of the Koum–Borindi granodiorite (c. 9 km), as assessed by the Al-in-hornblende geobarometer, suggests rapid exhumation rather than shallow emplacement. The pressure assessment of the metamorphism that affected the xenolith suggests that the Moho was at a depth of 25–28 km; hence, the crust was of normal thickness, ruling out any pre-obduction unroofing of the upper mantle, as well as long-term post-obduction crustal collapse.

Supplementary Materials: The following supporting information can be downloaded at: <https://www.mdpi.com/article/10.3390/min14050466/s1>, Table S1: whole rock geochemical data; Table S2: microprobe mineral data; Table S3: microprobe mineral data of amphiboles from granodiorite host rock used for pressure evaluation; Table S4: Nd–Sr isotope data for BOR5 xenolith and granodiorite host rock.

Author Contributions: Conceptualization, D.C.; investigation, D.C., F.T. and J.-L.P.; writing—original draft preparation, D.C. and F.T.; writing—review and editing, D.C. All authors have read and agreed to the published version of the manuscript.

Funding: This research received no external funding.

Data Availability Statement: All the data used in this study are freely available at Supplementary Materials.

Acknowledgments: The analytical work presented in this article was fully funded by the Institut des Sciences de la Terre d’Orléans (France) when D.C. was at the University of Orléans. We are grateful to the three reviewers for their constructive comments.

Conflicts of Interest: The authors declare no conflicts of interest.

References

1. Paris, J.P. *Géologie de la Nouvelle-Calédonie. Un Essai de Synthèse*; Mémoires du Bureau de Recherches Géologiques et Minières: Orléans, France, 1981; Volume 113, p. 278. ISBN 978-2-7159-5017-7.
2. Avias, J. Overthrust structure of the main ultrabasic New Caledonian massives. *Tectonophysics* **1967**, *4*, 531–541. [[CrossRef](#)]
3. Collot, J.Y.; Malahoff, A.; Recy, J.; Latham, G.; Missegue, F. Overthrust emplacement of New Caledonia Ophiolite: Geophysical evidence. *Tectonics* **1987**, *6*, 215–232. [[CrossRef](#)]
4. Cluzel, D.; Maurizot, P.; Collot, J.; Sevin, B. An outline of the Geology of New Caledonia; from Permian-Mesozoic Southeast-Gondwanaland active margin to Tertiary obduction and supergene evolution. *Episodes* **2012**, *35*, 72–86. [[CrossRef](#)]
5. Maurizot, P.; Cluzel, D.; Patriat, M.; Collot, J.; Iseppi, M.; Lesimple, S.; Secchiari, A.; Bosch, D.; Montanini, A.; Macera, P.; et al. Chapter 5: The Eocene Subduction-Obduction Complex of New Caledonia. In *New Caledonia: Geology, Geodynamic Evolution and Mineral Resources*; Maurizot, P., Mortimer, N., Eds.; Memoirs; Geological Society: London, UK, 2020; Volume 51. [[CrossRef](#)]
6. Dubois, J.; Launay, J.; Récy, J. Uplift movements in New Caledonia-Loyalty islands area and their plate tectonics interpretation. *Tectonophysics* **1974**, *24*, 133–150. [[CrossRef](#)]
7. Segev, A.; Rybakov, M.; Mortimer, N. A crustal model for Zealandia and Fiji. *Geophys. J. Int.* **2012**, *189*, 1277–1292. [[CrossRef](#)]
8. Klingelhofer, F.; Lafay, Y.; Collot, J.; Cosquer, E.; Géli, L.; Nouzé, H.; Vially, R. Crustal structure of the basin and ridge system west of New Caledonia (Southwest Pacific) from wide-angle and reflection seismic data. *J. Geophys. Res.* **2007**, *112*, 1–18. [[CrossRef](#)]
9. Régnier, M.; Van de Beuque, S.; Baldassari, C.; Tribot-Laspierre, G. La sismicité du Sud de la Nouvelle-Calédonie: Implications structurales. *Comptes Rendus Acad. Sci. Paris* **1999**, *329*, 931–932. [[CrossRef](#)]
10. Auzende, J.M.; Van de Beuque, S.; Régnier, M.; Lafay, Y.; Symonds, P. Origin of New Caledonian ophiolites based on a French-Australian seismic transect. *Marine Geol.* **2000**, *162*, 225–236. [[CrossRef](#)]
11. Hayes, D.E.; Ringis, J. Seafloor spreading in the Tasman Sea. *Nature* **1973**, *243*, 454–458. [[CrossRef](#)]
12. Gaina, C.; Müller, D.; Brown, B.; Ishihara, T. Microcontinent Formation around Australia. *Spec. Pap. Geol. Soc. Am.* **2003**, *372*, 405–416. [[CrossRef](#)]
13. Paquette, J.L.; Cluzel, D. U-Pb zircon dating of post-obduction volcanic-arc granitoids and a granulite xenolith from New Caledonia. Inference on Southwest Pacific Geodynamic Models. *Int. J. Earth Sci.* **2007**, *96*, 613–622. [[CrossRef](#)]
14. Cluzel, D.; Bosch, D.; Paquette, J.-L.; Lemennicier, Y.; Ménot, R.-P.; Montjoie, P. Late Oligocene post-obduction granitoids of New Caledonia (Southwest Pacific). A case for subduction reactivation and slab break-off. *Island Arc.* **2005**, *14*, 254–271. [[CrossRef](#)]
15. Marchesi, C.; Garrido, C.J.; Godard, M.; Belley, F.; Ferré, E. Migration and accumulation of ultra-depleted subduction-related melts in the Massif du Sud ophiolite (New Caledonia). *Chem. Geol.* **2009**, *266*, 171–186. [[CrossRef](#)]
16. Pirard, C.; Hermann, J.; O'Neill, H.S.C. Petrology and geochemistry of the crust-mantle boundary in a nascent arc, Massif du Sud Ophiolite, New Caledonia, SW Pacific. *J. Petrol.* **2013**, *54*, 1759–1792. [[CrossRef](#)]
17. Secchiari, A.; Montanini, A.; Bosch, D.; Macera, P.; Cluzel, D. The contrasting geochemical message from the New Caledonia gabbronorites: Insights on depletion and contamination processes of the sub-arc mantle in a nascent arc setting. *Contrib. Mineral. Petrol.* **2018**, *173*, 66. [[CrossRef](#)]
18. Pearce, J.A.; Harris, N.B.W.; Tindle, A.G. Trace element discrimination diagrams for the tectonic interpretation of granitic rocks. *J. Petrol.* **1984**, *25*, 956–983. [[CrossRef](#)]
19. Pearce, J.A. Sources and settings of granitic rocks. *Episodes* **1996**, *19*, 120–125. [[CrossRef](#)]
20. Mortimer, N.; Gans, P.B.; Palin, J.M.; Herzer, R.H.; Pelletier, B.; Monzier, M. Eocene and Oligocene basins and ridges of the Coral Sea-New Caledonia region: Tectonic link between Melanesia, Fiji, and Zealandia. *Tectonics* **2014**, *33*, 1386–1407. [[CrossRef](#)]
21. Nicholson, K.N.; Abu El-Rus, M.A. A case of Ampferer-type subduction beneath the New Caledonia arc: Evidence for inefficient subduction of hydrated lithologies into the upper mantle. *GSA Bull.* **2022**, *135*, 1139–1162. [[CrossRef](#)]
22. Moyen, J.F.; Janoušek, V.; Laurent, O.; Bachmann, O.; Jacob, J.B.; Farina, F.; Fiannacca, P.; Villaros, A. Crustal melting vs. fractionation of basaltic magmas: Part 1, granites and paradigms. *Lithos* **2021**, *402–403*, 106291. [[CrossRef](#)]
23. Jacob, J.B.; Moyen, J.F.; Fiannacca, P.; Laurent, O.; Bachmann, O.; Janoušek, V.; Farina, F.; Villaros, A. Crustal melting vs. fractionation of basaltic magmas: Part 2, Attempting to quantify mantle and crustal contributions in granitoids. *Lithos* **2021**, *402–403*, 106292. [[CrossRef](#)]

24. Defant, M.J.; Drummond, M.S. Derivation of some modern arc magmas by melting of young subducted lithosphere. *Nature* **1990**, *347*, 662–665. [[CrossRef](#)]
25. Richards, J.P.; Kerrich, R. Adakite-like rocks: Their diverse origins and questionable role in metallogenesis. *Econ. Geol.* **2007**, *102*, 537–576. [[CrossRef](#)]
26. Moyen, J.F. High Sr/Y and La/Yb ratios: The meaning of the “adakitic signature”. *Lithos* **2009**, *112*, 556–574. [[CrossRef](#)]
27. Sun, W.D.; Ling, M.X.; Chung, S.L.; Ding, X.; Yang, X.Y.; Liang, H.Y.; Fan, W.M.; Goldfarb, R.; Yin, Q.Z. Geochemical constraints on adakites of different origins and copper mineralization. *J. Geol.* **2012**, *120*, 105–120. [[CrossRef](#)]
28. Rapp, R.P.; Shimizu, N.; Norman, M.D.; Applegate, G.S. Reaction between slab-derived melts and peridotite in the mantle wedge: Experimental constraints at 3.8 GPa. *Chem. Geol.* **1999**, *160*, 335–356. [[CrossRef](#)]
29. Sevin, B.; Cluzel, D.; Maurizot, P.; Quesnel, F.; Ricordel-Prognon, C.; Chapronniere, G.; Folcher, N.; Quesnel, F. A drastic Lower Miocene regolith evolution triggered by post obduction slab break-off and uplift in New Caledonia. *Tectonics* **2014**, *33*, 1787–1801. [[CrossRef](#)]
30. Siivola, J.; Schmid, R. List of Mineral Abbreviations. Recommendations by the IUGS Subcommission on the Systematics of Metamorphic Rocks. Available online: <https://www2.bgs.ac.uk/scmr/products.html> (accessed on 1 February 2007).
31. Vidal, O.; Parra, T.; Trotet, F. A thermodynamic model for Fe-Mg aluminous chlorite using data from phase equilibrium experiments and natural pelitic assemblages in the 100–600 °C, 1–25 kbar range. *Am. J. Sci.* **2001**, *301*, 557–592. [[CrossRef](#)]
32. Trotet, F.; Vidal, O.; Jolivet, L. Exhumation of Syros and Sifnos metamorphic rocks (Cyclades, Greece). New constraints on the P-T paths. *Eur. J. Mineral.* **2001**, *13*, 901–920. [[CrossRef](#)]
33. Trotet, F.; Goffé, B.; Vidal, O.; Jolivet, L. Evidence of retrograde Mg-carpholite in the Phyllite-Quartzite nappe of Peloponnese from thermobarometric modelisation. Geodynamic implications. *Geodyn. Acta* **2006**, *19*, 323–343. [[CrossRef](#)]
34. Rieder, M.; Cavazzini, G.; D'Yakonov, Y.S.; Frank-Kamenetskii, V.A.; Gottardi, G.; Guoggenheim, S.; Koval, P.V.; Muller, G.; Neiva, A.M.R.; Radoslovich, E.W.; et al. Nomenclature of the micas. *Can. Mineral.* **1998**, *36*, 905–912. [[CrossRef](#)]
35. Nachit, H.; Ibhi, A.; Abia, E.H.; Ohoud, M.B. Discrimination between primary magmatic biotites, reequilibrated biotites and neoformed biotites. *C. R. Geosci.* **2005**, *337*, 1415–1420. [[CrossRef](#)]
36. Hey, M.H. A new review of the chlorites. *Mineral. Mag.* **1954**, *30*, 277–292.
37. Berman, R.G. Thermo barometry using multi-equilibrium calculations: A new technique, with petrological applications. *Can. Mineral.* **1991**, *29*, 833–855.
38. Vidal, O.; Parra, T. Thermodynamic constraints on the exhumation P-T paths of high-pressure metapelites based on chlorite-phengite local equilibrium. *Geol. Mag.* **2000**, *35*, 139–161. [[CrossRef](#)]
39. Bosse, V.; Ballèvre, M.; Vidal, O. The garnet isograds in the blueschist-facies metapelites of the Ile de Groix (Armorican Massif, France): A record of ductile thrusting during exhumation. *J. Petrol.* **2002**, *43*, 485–510. [[CrossRef](#)]
40. Árkai, P.; Faryad, S.W.; Vidal, O.; Balogh, K. Very low-grade metamorphism of sedimentary rocks of the Meliata unit, Western Carpathians, Slovakia: Implications of phyllosilicate characteristics. *Int. J. Earth Sci.* **2003**, *92*, 68–85. [[CrossRef](#)]
41. Rimmelé, G.; Parra, T.; Goffé, B.; Oberhansli, R.; Jolivet, L.; Candan, O. Exhumation Paths of High-Pressure–Low-Temperature Metamorphic Rocks from the Lycian Nappes and the Menderes Massif (SW Turkey): A Multi-Equilibrium Approach. *J. Petrol.* **2005**, *46*, 641–669. [[CrossRef](#)]
42. Evans, B.W. Phase relations in epidote-blueschists. *Lithos* **1990**, *25*, 3–23. [[CrossRef](#)]
43. Indares, A.; Martignole, J. Biotite-garnet geothermometry in the granulite facies: The influence of Ti and Al in biotite. *Am. Miner.* **1985**, *70*, 272–278.
44. Patino Douce, A.E. Titanium substitution in biotite: An empirical model with applications to thermometry, O₂ and H₂O barometries, and consequences for biotite stability. *Chem. Geol.* **1993**, *108*, 133–162. [[CrossRef](#)]
45. Schmidt, M.W. Amphibole composition in tonalite as a function of pressure: An experimental calibration of the Al-in-hornblende barometer. *Contrib. Mineral. Petrol.* **1992**, *110*, 304–310. [[CrossRef](#)]
46. Naney, M.T. Phase equilibria of rock-forming ferromagnesian silicates in granitic systems. *Am. J. Sci.* **1983**, *283*, 993–1033. [[CrossRef](#)]
47. Piwinski, A.J. Experimental studies of igneous rock series: Central Sierra Nevada batholith, California. *J. Geol.* **1968**, *76*, 548–570. Available online: <http://www.jstor.org/stable/i30066176> (accessed on 14 March 2007). [[CrossRef](#)]
48. Piwinski, A.J. Experimental studies of igneous rock series, central Sierra Nevada batholith, California: Part II. *Neues Jahrb. für Mineral.* **1973**, *5*, 193–215. [[CrossRef](#)]
49. Lambert, L.B.; Wyllie, P.J. Melting of tonalite and crystallization of andesite liquid with excess water to 30 kilobars. *J. Geol.* **1974**, *82*, 88–97. [[CrossRef](#)]
50. Castro, A. Tonalite–granodiorite suites as cotectic systems: A review of experimental studies with applications to granitoid petrogenesis. *Earth Sci. Rev.* **2013**, *124*, 68–95. [[CrossRef](#)]
51. Clemens, J.D. The granulite-granite connexion. In *Granulites and Crustal Evolution*; Vielzeuf, D., Vidal, P., Eds.; NATO ASI Series; Springer: Dordrecht, The Netherlands, 1990; Volume 311, pp. 25–36. [[CrossRef](#)]
52. McDonough, W.F.; Sun, S.; Ringwood, A.E.; Jagoutz, E.; Hofmann, A.W. Potassium, Rubidium and Cesium in the Earth and Moon and the evolution of the earth's mantle. *Geoch. Cosmoch. Acta* **1992**, *56*, 1001–1012. [[CrossRef](#)]
53. Zindler, A.; Hart, S. Chemical Geodynamics. *Annu. Rev. Earth Planet. Sci.* **1986**, *14*, 493–571. [[CrossRef](#)]

54. Chardon, D.; Chevillotte, V. Morphotectonic evolution of the New Caledonia ridge (Pacific Southwest) from post-obduction tectonosedimentary record. *Tectonophysics* **2006**, *420*, 473–491. [[CrossRef](#)]
55. Chevillotte, V.; Chardon, D.; Beauvais, A.; Maurizot, P.; Colin, F. Long-term tropical morphogenesis of New Caledonia (Southwest Pacific): Importance of positive epeirogeny and climate change. *Geomorphology* **2006**, *81*, 361–375. [[CrossRef](#)]
56. Cluzel, D.; Iseppi, M.; Chen, Y. Eocene pre- and syn-obduction tectonics in New Caledonia (Southwest Pacific). A case for oblique subduction, transcurrent tectonics and oroclinal bending; structural and paleomagnetic evidence. *Tectonophysics* **2021**, *811*, 228875. [[CrossRef](#)]

Disclaimer/Publisher’s Note: The statements, opinions and data contained in all publications are solely those of the individual author(s) and contributor(s) and not of MDPI and/or the editor(s). MDPI and/or the editor(s) disclaim responsibility for any injury to people or property resulting from any ideas, methods, instructions or products referred to in the content.